Measurements of pressure-induced $K\beta$ line shifts in ramp compressed cobalt up to 8 Mbar

S. Jiang,[1,*] A. E. Lazicki,[1] S. B. Hansen,[2] P. A. Sterne,[1] P. Grabowski,[1] R. Shepherd,[1] H. A. Scott,[1] R. F. Smith,[1] J. H. Eggert,[1] and Y. Ping[1]

[1]*Lawrence Livermore National Laboratory, Livermore, California 94550, USA*

[2]*Sandia National Laboratory, Albuquerque, New Mexico 87185, USA*

(Received 23 July 2019; accepted 17 December 2019; published 14 February 2020)

We report measurements of K-shell fluorescence lines induced by fast electrons in ramp-compressed Co targets. The fluorescence emission was stimulated by fast electrons generated through short-pulse laser-solid interaction with an Al target layer. Compression up to 2.1× solid density was achieved while maintaining temperatures well below the Fermi energy, effectively removing the thermal effects from consideration. We observed small but unambiguous redshifts in the $K\beta$ fluorescence line relative to unshifted Cu $K\alpha$. Redshifts up to 2.6 eV were found to increase with compression and to be consistent with predictions from self-consistent models based on density-functional theory.

DOI: 10.1103/PhysRevE.101.023204

I. INTRODUCTION

The electronic structure of warm dense matter (WDM) informs our understanding of material properties relevant to astrophysics, planetary science, and inertial confinement fusion applications. Under compression and heating, many-electron atoms can undergo both thermal and pressure ionization, which lead to a complex reorganization of their electronic structure. These changes in electronic structure can be revealed by measurements of x-ray emission and fluorescence lines.

Previous experiments have investigated the properties of warm and hot dense matter through both thermal and fluorescence emission measurements. Pioneering experiments in laser plasmas hinted at density-driven redshifts in the $1s$-$3p$ Heβ and Lyβ lines of hot laser-produced plasmas, and redshifts up to 6 eV in He-like Cl were recently definitively measured on the Orion laser facility [1] and found to be smaller than the redshifts predicted by an analytic model [2]. Pressure ionization was investigated in warm (180 eV) solid-density aluminum through fluorescence emission on Linac coherent light source (LCLS) [3] and found to be well described by a density-functional theory (DFT) model [4] but not by a collisional-radiative model with a standard treatment of ionization potential depression (IPD). In contrast, the standard IPD model was adequate to describe observed pressure ionization in hot compressed aluminum experiments on Orion [5]. Finally, a recent Z experiment [6] measured 5- to 12-eV shifts in both K-edge absorption and $K\beta$ fluorescence features with high-precision spectrometer from warm (∼10 eV) compressed (5×) iron; these shifts agreed well with DFT-based models.

In all these experiments, however, both thermal and compression effects had some impact on the inferred electronic structure. In this paper we report on an experiment that decouples density effects from thermal effects. Cobalt samples were ramp compressed to densities up to 2.1× solid (8.68 g/cm^3) while kept at temperatures below 1 eV, and fluorescence emissions were induced by fast electrons. The energy shifts of Co $K\beta$ lines were measured as a function of compression using a high-resolution x-ray spectrometer. Here we present details of the experiments and provide comparisons to both collisional-radiative models using various prescriptions for IPD and to self-consistent DFT-based models. We find good agreement between the experimental results and the DFT models and an incoherence in the collisional-radiative models with ad hoc density effects that may preclude their use as reliable tools to interpret data from dense plasmas with significant pressure effects on valence orbitals.

II. EXPERIMENT

A. Experimental setup

The experiment was performed at the OMEGA EP laser facility. A schematic of the experimental setup as well as the target structure is shown in Figs. 1(a) and 1(b). The target is made up of two parts. The primary part is a fluorescence layer sandwiched between two diamond plates. The material under study is a 20-μm Co foil, and an additional 4 μm Cu is inserted as an x-ray energy reference. The long UV pulses are incident from the right side of the target in Fig. 1(a), with a quasiramp pulse shape shown in Fig. 1(c). A similar technique has been demonstrated to compress Fe to 5 Mbar on OMEGA [7,8], where the same planar geometry was used to reach a 2× density while keeping the temperature below 1 eV. The diamond plates play a similar role as in the diamond anvil cell to confine the sample and maintain the pressure, thus creating a spatially uniform compression state in the fluorescence layer. The compression history is obtained via velocity interferometer system for any reflector (VISAR) in a separate shot without the short pulse as is shown in the inset of Fig. 1(a).

The change in ionization due to compression leads to variations in the energy levels of the material. These variations

*Corresponding author: jiang8@llnl.gov

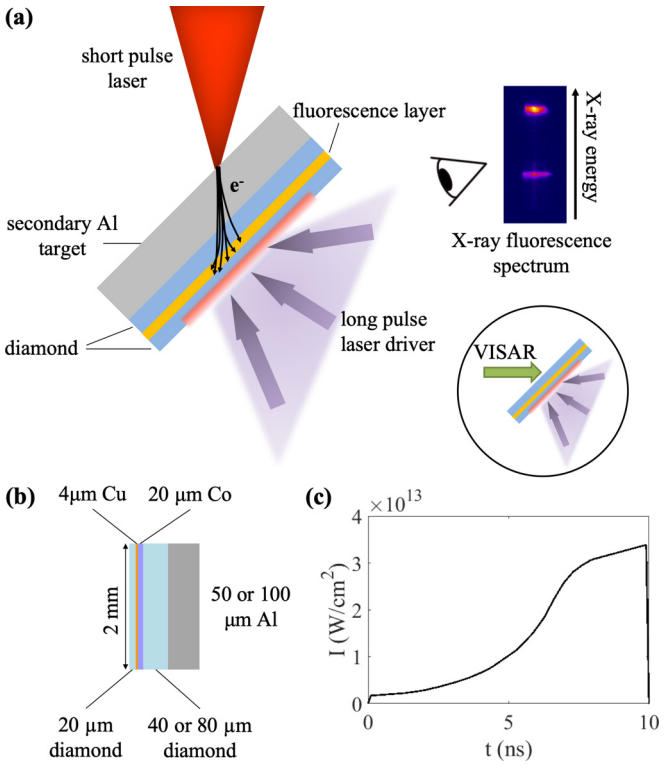

FIG. 1. Experimental setup. (a) A schematic of the experimental setup. The long pulse laser drivers are used to ramp compress the material. The fast electrons generated from the short pulse laser-solid interaction are used to induce K-shell fluorescence in the target. A typical raw image of the fluorescence spectrum (measured by IXTS) is shown on the right side. (b) Details of target. (c) Driver pulse shape for ramp compression.

can be detected by measuring the shifts of K-shell fluorescence lines. In order to induce fluorescence, a secondary, thick Al layer is attached to the other side of the primary target. It is irradiated by a short-pulse (ps scale), high-intensity ($>10^{18}$ W/cm^2) laser. A portion of the MeV electrons created via laser-solid interaction are able to transport through the secondary target. These electrons reaching the fluorescence layer can then induce $K\alpha$ and $K\beta$ emissions. The x-ray emission is measured using a one-dimensional (1D) spatially resolved high-resolution x-ray spectrometer [9,10].

A key feature in this experiment is that the low temperatures effectively eliminate thermal ionization effects. Co is close to Fe in Z, and the slow-ramp pulse shape in our experiment is expected to create a temperature similar to that in previous experiments [7,8]. We have performed hydrodynamic simulations which show that the temperature remains <1 eV under our driver laser conditions. The simulated electron temperatures are shown in Fig. 3(c) (see Sec. II C for more details). To prevent the hot electrons from heating up the fluorescence target, the volume of the secondary Al layer was chosen according to the previous study [11] using the same laser facility which shows that the temperature is determined by the laser energy and the target volume. It demonstrates that when the laser energy (J)/target volume (mm^3) is smaller than 10^4, the short-pulse laser does not heat up the target. During our experiment, the laser energy density ranges from 840 to 1223 J/mm^3, much lower than the 10^4 J/mm^3 threshold. Also, the measured Cu $K\beta/K\alpha$ ratio is at the cold material limit (0.14), which is further evidence that the fluorescence layer was kept at very low temperature during the experiment.

B. Material conditions

We employed two driver energies, 1500 J and 6600 J, to reach different densities. The ramp pulse is overall 10 ns long, with a peak intensity of 3.38×10^{13} W/cm^2 for 1500 J and 1.14×10^{14} W/cm^2 for 6600 J. The stress due to the driver is obtained from measurements of the free surface velocity of diamond using a line-imaging VISAR. The secondary Al target was removed from the primary target for VISAR measurements. The measured VISAR images are shown in Fig. 2(a), and the extracted velocity histories are shown in Fig. 2(b). VISAR A and B correspond to two different setups with different delays and sweep speeds in order to remove ambiguity due to 2π phase jumps. The short pulse probe time for 1500 J is 10.3 ns and for 6600 J is 10.0 ns. The corresponding spatially averaged pressure in Co as a function of time is shown in Fig. 2(c) with the spatial distribution inside the fluorescence layer displayed in the inset. The 4-μm Cu layer and the 20-μm Co layer are indicated with different colors. The pressures reach approximately 2 and 8 Mbar for the two driver conditions, respectively, and are quite uniform across the foils. The foil density is then obtained from the pressure using the isentropic compression curve. We have found from hydrodynamic simulations that the relation between density and pressure agrees well with the isentropic curve as shown in Fig. 3(d) (see Sec. II C for more details). In fact, the density falls into the region defined by Co isentropes with temperature T_e below 1 eV. In Fig. 2(d), the blue (lower) and green (upper) lines are isentropes corresponding to two different equation of state (EOS) models: The Livermore-based EOS and the SESAME EOS. The solid and dashed curves correspond to two different temperature ranges (<0.1 and <0.9 eV, respectively) which define the upper and lower bounds of the region. The yellow areas are the pressure range deducted from VISAR for the two driven conditions shown in Fig. 2(c). The black dots show the estimated compression with error bars. The compression reached about $1.5\times$ with 1500-J drive and $2.1\times$ with 6600-J drive.

C. Comparison with hydrodynamic simulations

To confirm the density measured from the experiment and get a further estimate of the temperature, we have done hydrodynamic simulations with the same target structures and driver conditions that have been used in the experiment. The simulations were performed using the HYADES code [12] with the Livermore-based EOS L270. The free surface velocities for the two driver energies (1500 J and 6600 J) from the simulations are compared to the VISAR measurements, as shown in Fig. 3. The simulations have reasonably reproduced the experimental results.

The spatially averaged electron temperature T_e in Co as a function of time from the simulations is displayed in Fig. 3(c). Both the 1500-J and 6600-J driver energy results show that the temperatures are below 1 eV during the whole compression process. Figure 3(d) shows the spatially averaged Co

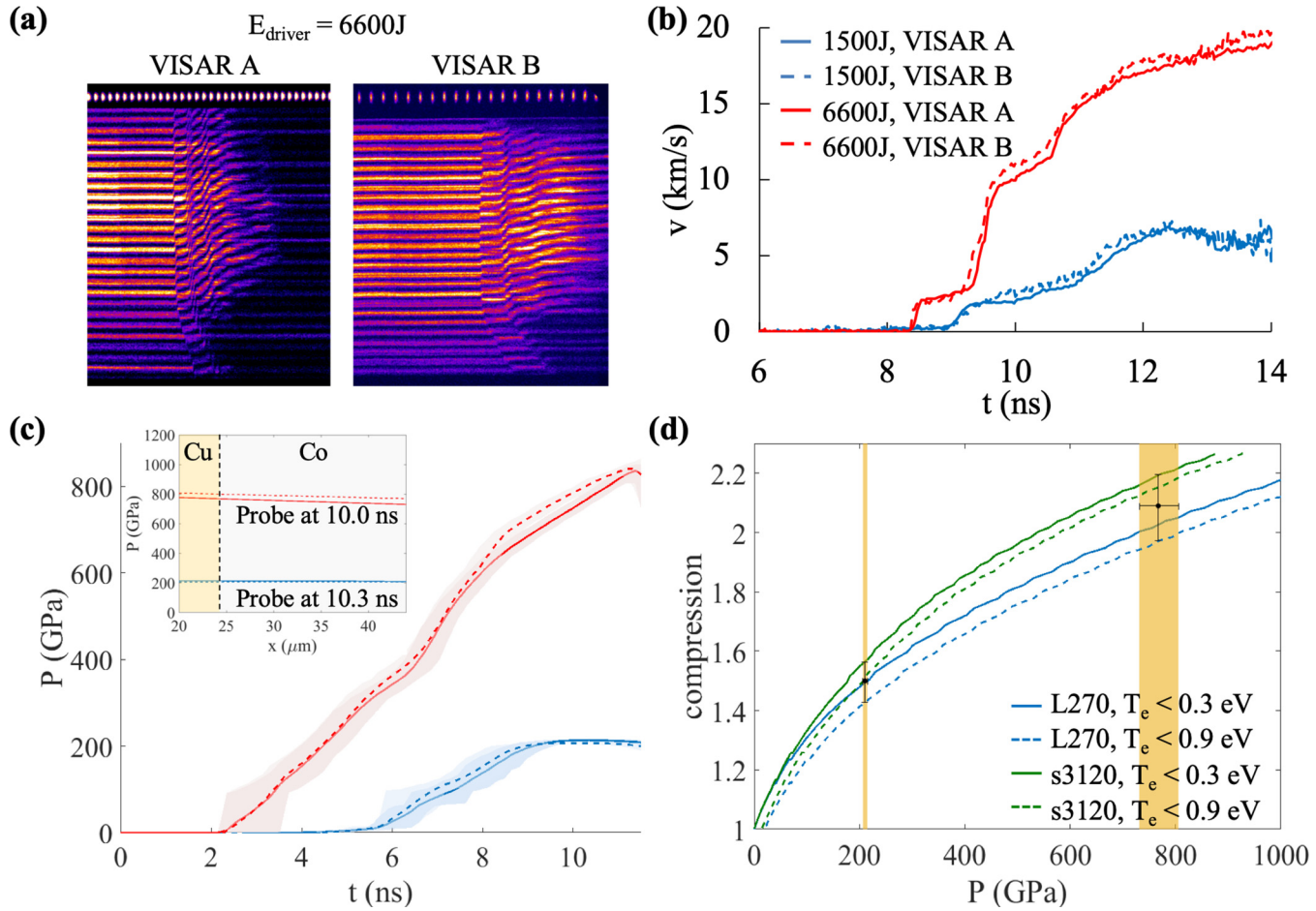

FIG. 2. Pressure and density measurements. (a) Raw VISAR images for 6600-J driver energy. (b) Extracted free surface velocity history for two different driver conditions. Blue (lower) curves are for 1500-J driver energy, and red (upper) curves are for 6600-J driver energy. (c) Average pressure in Co as a function of time, with the shaded areas showing the error bars. The results are derived from VISAR measurements. The short pulse probe arrives at 10.3 ns for 1500 J and 10.0 ns for 6600 J of driver energy. Pressure reaches about 2 and 8 Mbar, respectively. Pressure distribution across the Cu and Co layer at the time of the short pulse probe is shown in the inset. (d) Inferred compression using Co isentrope. The blue (lower) and green (upper) curves are from two different models: The Livermore-based EOS (L270) and the Sesame table (s3120). The solid curves show the isentropes from very low temperatures (<0.3 eV), while the dashed curves are from slightly higher temperatures (but still <0.9 eV). The compression is confined within the upper and lower bounds defined by the green solid curve and blue dashed curve.

compression vs. pressure extracted from the two simulations. The simulated results actually fall on the isentropic curve of Co. This further justifies that we can get Co compression using the isentropic curve and the experimentally measured pressure.

D. Fluorescence spectra

The fluorescence spectra were measured using a high-resolution imaging X-ray Thomson scattering spectrometer (IXTS) [9,10]. It spans an energy range from ~7550 to ~8050 eV with a spectral resolution of about 3 eV. Both the Cu $K\alpha$ and Co $K\beta$ emissions are within this range. Calculations from multiple models indicate that the shift in Cu $K\alpha$ that originates from density changes is much smaller than that in Co $K\beta$. DFT-based models, which we will show later in the text, are in the best agreement with data, suggesting that there is only a small shift in Cu $K\alpha$ (<1 eV) from 1× to 2.5× compression. This is because the $K\alpha$ ($2p \rightarrow 1s$) transition has a deeply bound initial state that is less sensitive to density effects than the $K\beta$ ($3p \rightarrow 1s$) transition, whose upper level lies much closer to the continuum. Here we employ Cu $K\alpha$ as a spectral fiducial and measure the relative shift in Co $K\beta$. The Co spectra under different compressions are shown in Fig. 4. In Fig. 4(a), the Co $K\beta$ peaks are normalized with respect to the maximum intensity of the Cu $K\alpha$ peaks, while in Fig. 4(b), they are normalized to 1. We have observed a small redshift that is about −3 eV from 1× to ~2.0–2.2× compression, as well as broadening and suppression in the Co $K\beta$ peak. In comparing the measured spectra to predictions using various ionization models and atomic codes in the next section, both the Co $K\beta$ and Cu $K\alpha$ lines at different compressions are calculated, and the relative energy shifts are compared with the experimental result.

III. MODELS AND COMPARISON TO EXPERIMENT

Collisional-radiative models (e.g., CRETIN [13], FLYCHK [14], LASNEX-DCA [15], SCSF [16,17], SCRAM [18],

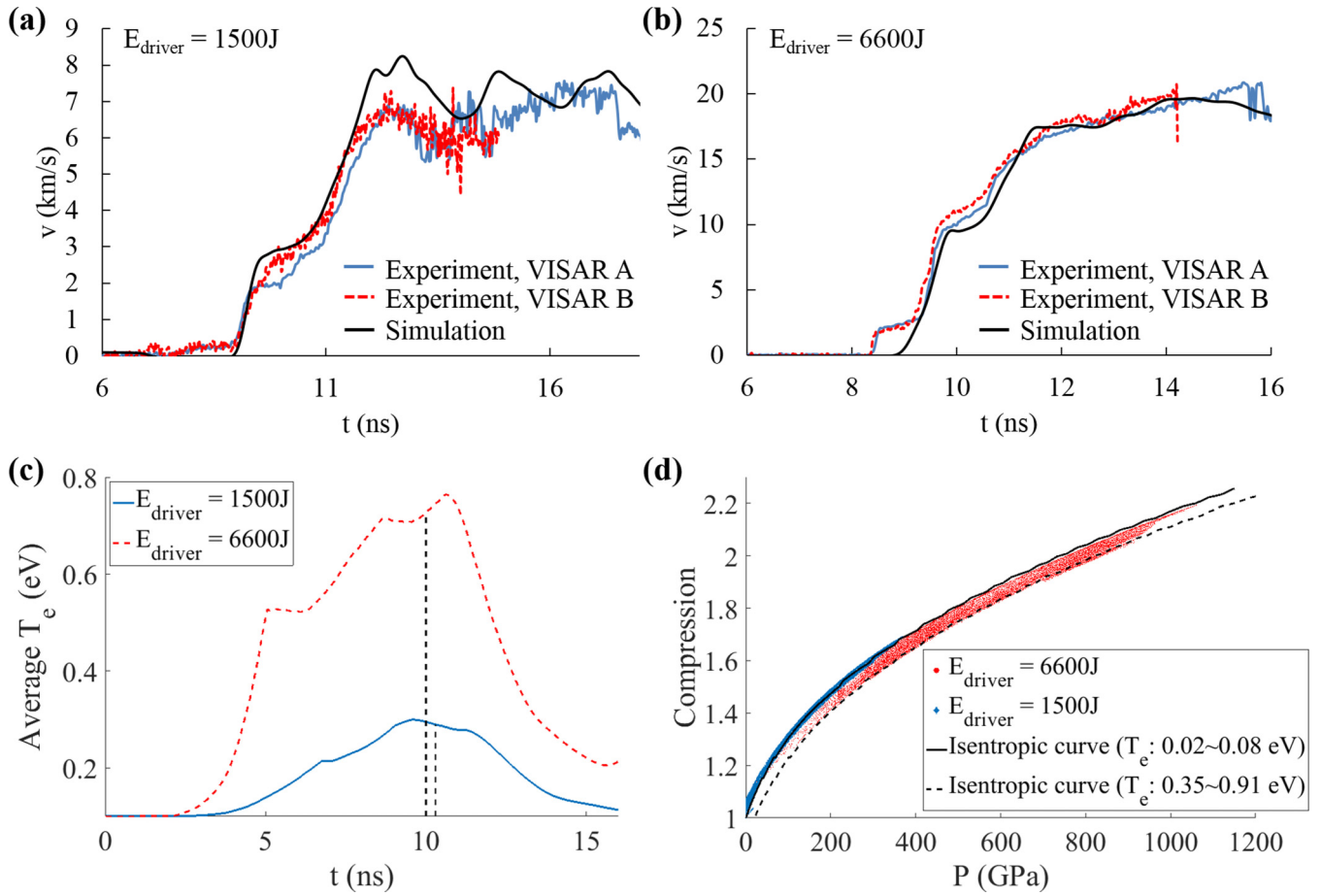

FIG. 3. Results from hydrodynamic simulations (a); panel (b) compares free surface velocity from hydrodynamic simulation to that from experiment. Panels (a) and (b) correspond to two different driver energies: 1500 J and 6600 J. The black curve shows the result from HYADES simulation, while and blue and red curves are the VISAR measurements from the experiment. The simulation results agree reasonably well with the experiment. Panels (c) and (d) shows the spatially averaged Co temperature, compression, and pressure from hydrodynamic simulations. (c) Spatially averaged electron temperature in Co as a function of time for driver energies 1500 J (blue, solid) and 6600 J (red, dashed). The dashed black curves indicate the probe time for these two driver conditions. (d) Spatially averaged compression vs. pressure in Co at different time in the simulations. The blue diamonds and red dots are from different simulations with 1500 J and 6600 J driver energies, respectively. The black line is the isentropic curve from the L270 EOS model. The result demonstrates that the relation between average density and average pressure follows the isentropic curve.

etc.), are typically based on isolated-ion electronic structure that can be modified at high densities by continuum lowering (or ionization potential depression) models such as Stewart-Pyatt (SP) [19] or Ecker-Kroll (EK) [20]. As density increases and an ion's bound states move closer to (and eventually merge with) the continuum, these prescriptions for pressure ionization can introduce sharp discontinuities in the calculated Z^* when an occupied valence state is destroyed. For example, the Z^* of cold Co would change from 0 to 9 under pressure ionization of its valence $3d$ shell. Some collisional-radiative models smooth out this effect by gradually decreasing statistical weights in states near the continuum, but the precise implementation tends to be particular to individual models [21]. Predictions for line emission from these models can be complex: Both IPD and thermal effects can increase the average ion charge state Z^*, which tends to reduce screening and increase the energies of line emission from particular transitions. But density shifts that tend to counteract this increase can be introduced by appealing to ad hoc models such as the ones described by Nguyen *et al.* [22] or Li *et al.* [2]. These line-shift models are not formally consistent with the IPD models that influence Z^* and are also deployed somewhat idiosyncratically among existing collisional-radiative models.

By contrast, models based on DFT (e.g., Purgatorio [23,24]) treat all electrons quantum mechanically and self-consistently, varying orbital energies and wave functions with the plasma conditions. Figure 5(a) gives a DFT model density of states for solid-density cobalt. Where the $3s$ and $3p$ orbitals have negative energies and are represented by δ functions, the pressure-ionized valence $3d$ orbital forms a resonance at $+8$ eV that corresponds roughly to a d band in the metal. Filling the total density of states up to the calculated Fermi energy of 11 eV leads to a Z^* of 9. However, filling only the ideal density of states, which excludes the resonance, gives a Z^* of 1.8, which is consistent with solid-state theory

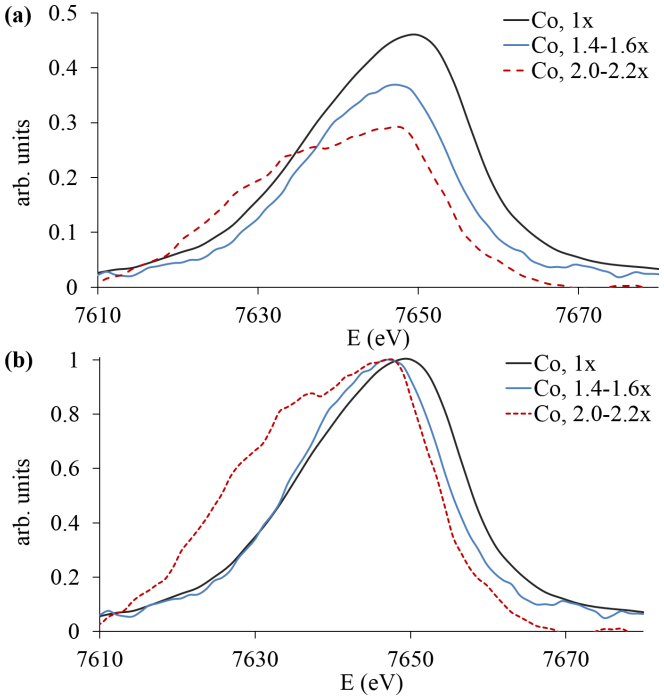

FIG. 4. The Co $K\beta$ spectra as a function of compression. The energies in the plots are labeled assuming that Cu $K\alpha$ does not shift and the Co $K\beta$ peak energy is calibrated with respect to Cu $K\alpha$. (a) The curves are normalized with respect to the peak intensities of Cu $K\alpha$ under the same conditions. (b) The curves are normalized with respect to their peaks.

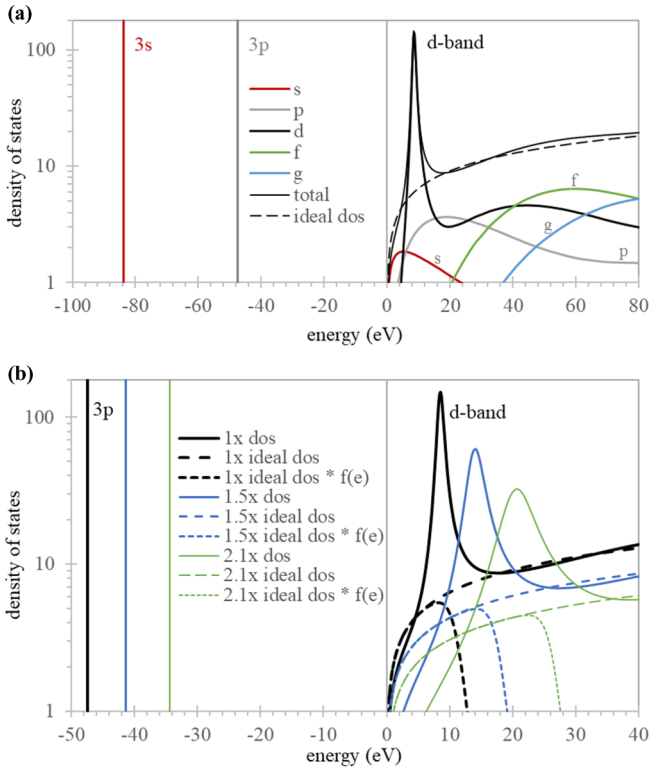

FIG. 5. Electronic density of states (dos) from an average-atom (DFT) model. (a) The $3s$ and $3p$ orbitals are bound in solid density Co, while the continuum density of states includes near-ideal contributions from all angular momentum channels except $\ell = 2$, which forms a narrow d-band resonance from the residual of the pressure-ionized $3d$ orbital. (b) Under compression, the bound states move closer to the continuum and the d-band resonance moves up in energy along with the Fermi energy. Z^* is given by integrating the ideal electron density of states modulated by the Fermi distribution $f(e)$ over energy.

and typical carrier electron densities of cold transition metals. Z^* is thus seen to be a problematic quantity for both collisional-radiative and DFT-based models (as discussed in Murillo *et al.* [25]). However, edge energies and line shifts are much less problematic from DFT-based models than from colisional-radiative models. The lower panels of Fig. 5 illustrate that under compression, all of the critical energies (3ℓ binding energies, d-band resonance energy, and the Fermi energy) shift up in energy by almost (but not exactly) the same amount. These differential changes in energies provide native shifts in ionization potentials and line emission energies without the necessity of appealing to ad hoc modifications to isolated-atom electronic structure.

Mean ionization values at the experimental compressions are given in Table I from a variety of collisional-radiative and DFT-based models. Both types of models predict that Z^* should increase with compression. The two DFT-based models agree well with each other (as expected, since only the relativistic treatment differs between the models). Both show modest changes in Z^* under compression. The collsional-radiative models also predict increasing Z^* under compression but have higher Z^* than the DFT models at all compressions and large variations between models. The differences due to using different underlying structure and IPD implementation (which vary between models) are similar to the differences due to different choices in IPD theory (SP or EK). However, in general the collisional-radiative models predict larger ionization with EK than with SP.

The incoherence of the ad hoc density effect required by collisional-radiative models is increased when line shifts are considered, so comparison to the observable quantity reported here (the change in the Co $K\beta$ fluorescence energy relative to Cu $K\alpha$) is conflated with many choices that can reasonably differ among models. We might interpret the number of bound electrons $\mathrm{Zb} = \mathrm{Zn} - Z^*$ as a complete picture of screening, thus associating changes in Z^* with shifts in Co $K\beta$. Depending on the particular electronic structure of the collisional-radiative models and the calculated Z^*, we find 1- to 4-eV blueshifts per ionized $3d$ electron. In this interpretation, a redshift in Co $K\beta$ under compression implies a decrease in Z^*, inconsistent with all predictions in Table I. Adding density-dependent plasma polarization shifts from Nguyen *et al.* [22] of about -1 eV per charge state to the collisional-radiative models moderates this conclusion, but even with this second-order correction, none of the collisional-radiative models are consistent with the measured data.

This incoherence is illustrated in Fig. 6, which shows Z^*-dependent Co $K\beta$ and Cu $K\alpha$ shifts along with measured and modeled Co $K\beta$ energy shifts with respect to Cu $K\alpha$ as a function of compression. Here CRETIN and FLYCHK with

TABLE I. Mean ionization state Z^* predicted by various models.

Compression	1×	1.5×	2.1×
	Collisional-radiative models		
CRETIN [13] + SP [19]	5.0	6.0	8.0
CRETIN [13] + EK [20]	9.0	9.0	17.0
FLYCHK [14] + SP [19]	4.0	6.0	7.0
FLYCHK [14] + EK [20]	9.0	9.0	17.0
SCSF [16,17] + SP [19]	3.0	3.0	4.0
SCSF [16,17] + EK [20]	5.0	6.0	8.0
SCRAM [18] + SP [19]	3.0	3.0	4.0
SCRAM [18] + EK [20]	5.0	6.0	8.0
	DFT-based models		
Purgatorio [23,24]	1.8	2.5	3.3
MUZE	1.8	2.5	3.2

EK both predict strong relative redshifts at 1.5× compression and then the complete destruction of M shell states at 2.1× compression, which would lead to no $K\beta$ emission at all. SCSF and SCRAM with EK predict large blueshifts (17.7 and 14.7 eV, respectively) at 2.1× compression that are inconsistent with the measurements and a significant reduction in the $3p$ statistical weight that would significantly weaken the Co $K\beta$ line. With SP, the four different codes predict smaller ionization and significant blueshifts that remain inconsistent with the measurements. Given the large variations among models and the inability of any such variation to match the measured data, caution should clearly be taken when using collisional-radiative models to draw conclusions about the ionization stage of warm dense matter or the validity of any particular IPD theory.

The DFT-based models, however, provide direct predictions for the change in $K\alpha$ and $K\beta$ emission energies under compression, and their predictions follow the measured shifts within the experimental error bars. As implied by the close agreement of two independent implementations, the energy separation between electronic orbitals in these models is highly constrained due to the internal coherence of the underlying models and the absence of appeals to external ad hoc prescriptions. The difficulty with these models is that, because the DFT orbitals are fictitious average states that do not account for multiple detailed configurations, they tend to have poor "absolute" agreement with precisely measured fluorescence-line transition energies for cold materials. However, initial Hartree-Fock calculations indicate that these multiconfiguration effects impact different compressions in similar ways, so that the predicted changes in the Co $K\beta$ and Cu $K\alpha$ separation are meaningful as reflections of the balance between increasing pressure ionization (which reduces screening of the nuclear charge by bound electrons) and increasing pressure from the pressure-ionized electrons (which increases screening of the nuclear charge by free electrons). The fact that a redshift is observed indicates that the increase in free-electron screening has a slightly greater impact than the reduction of bound-electron screening. This is also consistent with the results shown by Hansen *et al.* in the Z experiment [6].

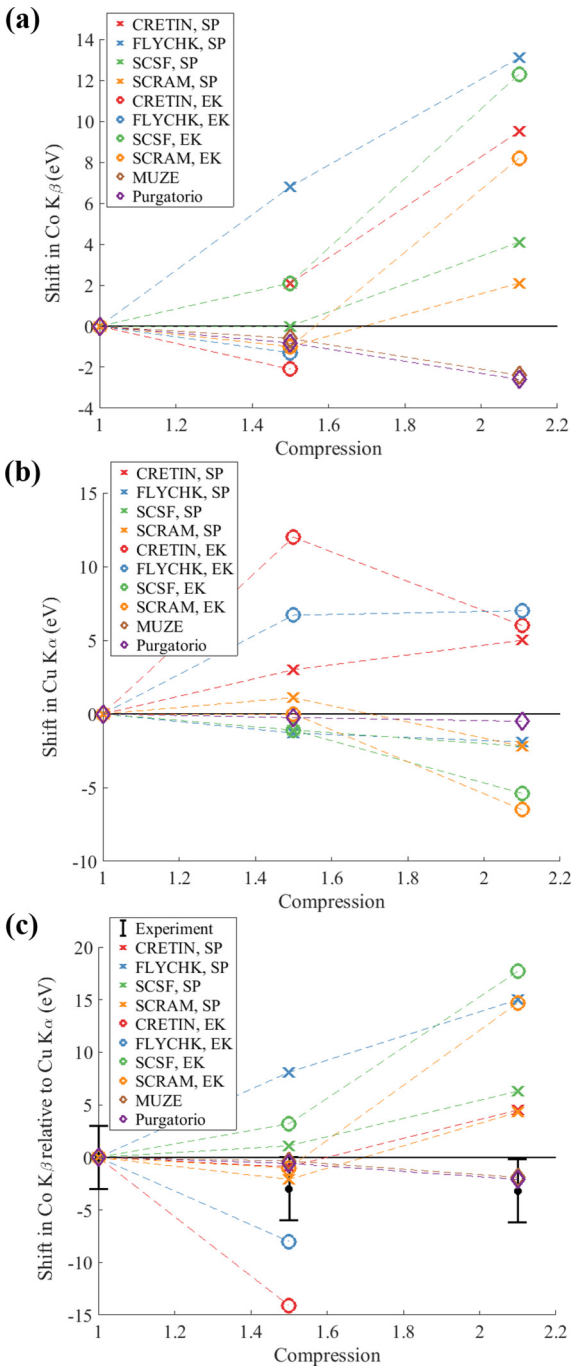

FIG. 6. Shift in Co $K\beta$ and Cu $K\alpha$ from different models. (a) Shift in Co $K\beta$ as a function of compression with different models. At 2.1× compression, the isolated-atom models all predict blueshifts while the average-atom models predict redshifts. Note that there are no data at 2.1× compression for CRETIN + EK and FLYCHK + EK, because the $3p$ state is pressure ionized according to these models. (b) Shift in Cu $K\alpha$ as a function of compression. (c) Compare the shift of the energy difference between Co $K\beta$ and Cu $K\alpha$ from experiment (black dot with error bars) to predictions from various models, including CRETIN + SP (red "x"), FLYCHK + SP (blue "x"), SCSF + SP (green "x"), SCRAM + SP (orange "x"), CRETIN + EK (red circle), FLYCHK + EK (blue circle), SCSF + EK (green circle), SCRAM + EK (orange circle), MUZE (nonrelativistic version of Purgatorio, brown diamond) and Purgatorio (purple diamond).

IV. CONCLUSIONS

We have described a method to study the electronic structure of a transition metal as a function of mass density. Using ramp compression to increase the density of the material while keeping the temperature below 1 eV, we have isolated density effects from thermal effects. Our measurements of K-shell fluorescence lines induced by fast electrons generated through short-pulse laser-solid interaction show a small but unambiguous decrease in the energy separation of Co $K\beta$ and Cu $K\alpha$, which increases with compression. We found a fundamental incoherence in attempts to compare these results with multiple independent collisional-radiative models, each of which has a different implementation of ad hoc density effects. We found good agreement of the measured data with two independent implementations of models based on density-functional theory.

ACKNOWLEDGMENTS

We thank the OMEFA EP team for laser operation and technical support. This work was performed under the auspices of the U.S. Department of Energy by Lawrence Livermore National Laboratory under Contract No. DE-AC52-07NA27344 with support from the LLNL LDRD program and DOE OFES Early Career program. Sandia National Laboratories is a multimission laboratory managed and operated by National Technology and Engineering Solutions of Sandia, LLC, a wholly owned subsidiary of Honeywell International, Inc., for the U.S. Department of Energy's National Nuclear Security Administration under Contract No. DE-NA-0003525. The work of SBH was supported by the U.S. Department of Energy, Office of Science Early Career Research Program, Office of Fusion Energy Sciences under Grant No. FWP-14-017426.

[1] P. Beiersdorfer, G. V. Brown, A. McKelvey, R. Shepherd, D. J. Hoarty, C. R. D. Brown, M. P. Hill, L. M. R. Hobbs, S. F. James, J. Morton, and L. Wilson, Phys. Rev. A **100**, 012511 (2019).

[2] X. Li and F. B. Rosmej, Europhys. Lett. **99**, 33001 (2012).

[3] O. Ciricosta, S. M. Vinko, H.-K. Chung, B.-I. Cho, C. R. D. Brown, T. Burian, J. Chalupsky, K. Engelhorn, R. W. Falcone, C. Graves, V. Hajkova, A. Higginbotham, L. Juha, J. Krzywinski, H. J. Lee, M. Messerschmidt, C. D. Murphy, Y. Ping, D. S. Rackstraw, A. Scherz, W. Schlotter, S. Toleikis, J. J. Turner, L. Vysin, T. Wang, B. Wu, U. Zastrau, D. Zhu, R. W. Lee, P. Heimann, B. Nagler, and J. S. Wark, Phys. Rev. Lett. **109**, 065002 (2012).

[4] S. Vinko, O. Ciricosta, and J. Wark, Nat. Commun. **5**, 3533 (2013).

[5] D. J. Hoarty, P. Allan, S. F. James, C. R. D. Brown, L. M. R. Hobbs, M. P. Hill, J. W. O. Harris, J. Morton, M. G. Brookes, R. Shepherd, J. Dunn, H. Chen, E. VonMarley, P. Beiersdorfer, H. K. Chung, R. W. Lee, G. Brown, and J. Emig, Phys. Rev. Lett. **110**, 265003 (2013).

[6] S. B. Hansen, E. C. Harding, P. F. Knapp, M. R. Gomez, T. Nagayama, and J. E. Bailey, High Energy Density Phys. **24**, 39 (2017).

[7] Y. Ping, F. Coppari, D. G. Hicks, B. Yaakobi, D. E. Fratanduono, S. Hamel, J. H. Eggert, J. R. Rygg, R. F. Smith, D. C. Swift, D. G. Braun, T. R. Boehly, and G. W. Collins, Phys. Rev. Lett. **111**, 065501 (2013).

[8] Y. Ping, D. G. Hicks, B. Yaakobi, F. Coppari, J. Eggert, and G. Collins, Rev. Sci. Instrum. **84**, 123105 (2013).

[9] E. J. Gamboa, D. S. Montgomery, I. M. Hallc, and R. P. Drake, J. Instrum. **6**, P04004 (2011).

[10] E. J. Gamboa, C. M. Huntington, M. R. Tranthan, P. A. Keiter, R. P. Drake, D. S. Montgomery, J. F. Benage, and S. A. Letzring, Rev. Sci. Instrum. **83**, 10E108 (2012).

[11] P. M. Nilson, A. A. Solodov, J. F. Myatt, W. Theobald, P. A. Jaanimagi, L. Gao, C. Stoeckl, R. S. Craxton, J. A. Delettrez, B. Yaakobi, J. D. Zuegel, B. E. Kruschwitz, C. Dorrer, J. H. Kelly, K. U. Akli, P. K. Patel, A. J. Mackinnon, R. Betti, T. C. Sangster, and D. D. Meyerhofer, Phys. Rev. Lett. **105**, 235001 (2010).

[12] J. T. Larsen and S. M. Lane, J. Quant. Spectr. Rad. Transf. **51**, 179 (1994).

[13] H. A. Scott, J. Quant. Spectrosc. Radiat. Transf. **71**, 689 (2001).

[14] H. K. Chung, M. Chen, W. Morgan, Y. Ralchenko, and R. Lee, High Energy Density Phys. **1**, 3 (2005).

[15] Y. T. Lee, J. Quant. Spectrosc. Radiat. Transf. **38**, 131 (1987).

[16] H. A. Scott and S. B. Hansen, High Energy Density Phys. **6**, 39 (2010).

[17] S. B. Hansen, J. Bauche, and C. Bauche-Arnoult, High Energy Density Phys. **7**, 27 (2011).

[18] S. B. Hansen, J. Bauche, C. Bauche-Arnoult, and M. F. Gu, High Energy Density Phys. **3**, 109 (2007).

[19] J. Stewart and K. D. Pyatt, Astrophys. J. **144**, 1203 (1966).

[20] G. Ecker and W. Kroll, Phys. Fluids **6**, 62 (1963).

[21] S. B. Hansen, H.-K. Chung, C. J. Fontes, Y. Ralchenko, H. A. Scott, and E. Stambulchik, High Energy Density Physics **35**, 100693 (2019).

[22] H. Nguyen, M. Koenig, D. Benredjem, M. Caby, and G. Coulaud, Phys. Rev. A **33**, 1279 (1986).

[23] B. Wilson, V. Sonnad, P. Sterne, and W. Isaacs, J. Quant. Spectrosc. Radiat. Transf. **99**, 658 (2006).

[24] P. A. Sterne, S. B. Hansen, B. G. Wilson, and W. A. Isaacs, High Energy Density Phys. **3**, 278 (2007).

[25] M. S. Murillo, J. Weisheit, S. B. Hansen, and M. W. C. Dharma-wardana, Phys. Rev. E **87**, 063113 (2013).